Chinese Chemical Letters 36 (2025) 110042

Contents lists available at ScienceDirect

Chinese Chemical Letters

journal homepage: www.elsevier.com/locate/cclet

Morphology engineering and electronic structure remodeling of manganese-incorporated VN for boosting urea-assisted energy-saving hydrogen production

Hongyang Li[a], Yue Liu[a], Xiuwen Wang[b], Haijing Yan[a,*], Guimin Wang[a], Dongxu Wang[a], Yilong Wang[a], Shuo Yang[a], Yanqing Jiao[a,*]

[a] Key Laboratory of Functional Inorganic Material Chemistry, Ministry of Education of the People's Republic of China, Heilongjiang University, Harbin 150080, China

[b] Heilongjiang Provincial Key Laboratory of Surface Active Agent and Auxiliary, School of Chemistry and Chemistry Engineering, Qiqihar University, Qiqihar 161006, China

ARTICLE INFO

Article history:
Received 7 April 2024
Revised 3 May 2024
Accepted 22 May 2024
Available online 23 May 2024

Keywords:
Morphology engineering
Electronic structure regulation
Metal nitrides
Hydrogen evolution reaction
Urea oxidation reaction

ABSTRACT

Urea-assisted water electrolysis offers a promising route to reduce energy consumption for hydrogen production and meanwhile treat urea-rich wastewater. Herein, we devised a shear force-involved polyoxometalate-organic supramolecular self-assembly strategy to fabricate 3D hierarchical porous nanoribbon assembly Mn-VN cardoons. A bimetallic polyoxovanadate (POV) with the inherent structural feature of Mn surrounded by [VO_6] octahedrons was introduced to trigger precise Mn incorporation in VN lattice, thereby achieving simultaneous morphology engineering and electronic structure modulation. The lattice contraction of VN caused by Mn incorporation drives electron redistribution. The unique hierarchical architecture with modulated electronic structure that provides more exposed active sites, facilitates mass and charge transfer, and optimizes the associated adsorption behavior. Mn-VN exhibits excellent activity with low overpotentials of 86 mV and 1.346 V at 10 mA/cm^2 for hydrogen evolution reaction (HER) and urea oxidation reaction (UOR), respectively. Accordingly, in the two-electrode urea-assisted water electrolyzer utilizing Mn-VN as a bifunctional catalyst, hydrogen production can occur at low voltage (1.456 V@10 mA/cm^2), which has the advantages of energy saving and competitive durability over traditional water electrolysis. This work provides a simple and mild route to construct nanostructures and modulate electronic structure for designing high-efficiency electrocatalysts.

© 2025 Published by Elsevier B.V. on behalf of Chinese Chemical Society and Institute of Materia Medica, Chinese Academy of Medical Sciences.

Faced with severe energy crisis and environmental pollution, significant efforts have been dedicated to exploring renewable and eco-friendly energy sources [1]. Hydrogen has emerged as a compelling energy carrier because of its high energy density, environmental friendliness, and sustainability [2,3]. Compared with traditional industrial hydrogen production methods (coal gasification and steam methane reforming), electrocatalytic water splitting technique that can produce "green hydrogen" has garnered significant research attention [4,5]. Unfortunately, the energy efficiency of water electrolysis is limited by the slower kinetics of oxygen evolution reaction (OER) [6,7]. Recently, more thermodynamic favorable oxidations of small organic molecules (*e.g.*, methanol, hydrazine, and urea) have been investigated as alternatives to reduce energy consumption [8,9]. Among these, urea oxidation reaction (UOR) with the low theoretical potential of 0.37 V is compelling, because UOR-assisted water electrolysis can theoretically achieve 70% energy saving, while alleviating the dilemma of urea-rich wastewater pollution [10,11]. Nevertheless, UOR still faces challenge in higher potential input requirements, mainly due to its complex and slow six-electron transfer process involving the adsorption/desorption of multi-step intermediates [12,13]. Although noble metal catalysts (*e.g.*, Pt, Ru, and Au) shows catalytic activity toward UOR, their high cost and limited reserves are the incentives to develop cost-efficient and durable electrocatalysts [14].

Transition metal nitrides (TMNs) have become one of the promising alternatives to noble-metal catalysts in various catalysis fields, because of their Pt-like electronic structure, high conductivity and chemical stability [15]. Especially, vanadium nitride (VN) with the characteristic of multiple oxidation states, superior electrical conductivity (1.17×10^6 S/m), and excellent electrochem-

* Corresponding authors.
E-mail addresses: yanhaijing@hlju.edu.cn (H. Yan), jiaoyanqing@hlju.edu.cn (Y. Jiao).

https://doi.org/10.1016/j.cclet.2024.110042
1001-8417/© 2025 Published by Elsevier B.V. on behalf of Chinese Chemical Society and Institute of Materia Medica, Chinese Academy of Medical Sciences.

ical durability has attracted extensive attention in electrochemical energy storage and conversion [16]. However, unitary VN usually exhibits inadequate HER/OER activity, on account that large density unoccupied d-orbital of V ($3d^3 4s^2$) induces strong charge interactions between VN and reaction intermediates. The absorption energy of different intermediates can be optimized by adjusting the electronic structure [17]. In this regard, the integration of electron-rich late transition metals into VN has emerged as an effective way to trigger electronic redistribution based on "3d orbital electron complementarity effect" [18]. Our previous work has indicated that V-Co (Ni)-based bimetallic compounds have excellent HER and OER performances where synergistic effect regulates the adsorption energy of intermediates [19-21]. Recently, manganese (Mn) is deemed as an ideal modulator for customizing electronic structures owing to its variable valence states, abundant reserves and low cost [22]. Especially, Mn^{3+} in $t^3_{2g}e^1_g$ electronic configuration with Jahn-Teller distortion has been proposed to favor water adsorption, and function as an important active site for water oxidation [23-26]. For UOR, it was verified that Mn-doping promoted the adsorption of urea and the desorption of CO_2 [27,28]. Motivated by this point, incorporating Mn atom into VN is predicted to simultaneously achieving high activity towards UOR and HER, but is relatively unexplored. Beyond electronic structure modulation, morphology engineering is also a pivotal tool to improve catalytic activity [29]. Two-dimensional (2D) porous nanosheets with largely exposed surface atoms can increase the number of active sites and facilitate mass transfer [30-32]. Especially, three-dimensional (3D) hierarchical architectures assembled from nanosheets inherit the structural advantage and related catalytic activity from nanosheets while guaranteeing durability during electrocatalysis [33,34]. Accordingly, constructing 3D porous hierarchical structured Mn-doped VN is highly desirable but challenging, considering that VN tends to aggregate into large particles during high-temperature treatment [35].

Enlighted by our previous work of constructing 2D Mo-based nanosheet precursors based on polyoxometalate (POM) assembly [36], a polyoxovanadate $(NH_4)_7[MnV_{13}O_{38}]\cdot 18H_2O$ ($[MnV_{13}]$ for short) is expected to trigger precise Mn doping in the VN lattice, enabling morphology engineering and electronic structure regulation of VN. Herein, we devised a shear force-involved molecular self-assembly of melamine (MA) and $[MnV_{13}]$ to construct a hierarchical structure precursor (denoted as $[MnV_{13}]$-MA) composed of nanoribbons. After controllable nitridation, a 3D hierarchical nanoribbon-assembled flower-like Mn-doped VN (aliased as Mn-VN) was fabricated. The incorporation of Mn into the VN lattice resulted in lattice contraction, which is expected to tune the electronic structure of the VN for promoting the relevant adsorption behavior. Remarkably, Mn-VN catalyst exhibited an enhanced electrocatalytic performance in both HER and UOR, achieving 86 mV and 1.346 V at 10 mA/cm^2, and its durability reached 100 h and 60 h, respectively, due to the 3D porous hierarchical assembly architecture that Mn-VN nanoparticles were embedded in thin carbon layers. Significantly, the assembled urea-assisted hydrogen production electrolytic cell only needs 1.456 V to reach 10 mA/cm^2, underscoring its significant potential for energy-efficient hydrogen production from urea-rich wastewater.

The synthetic procedure of 3D hierarchical nanoribbon-assembled Mn-VN cardoon is schematically illustrated in Fig. 1a. Briefly, shear-stress-modulated self-assembly of MA and $[MnV_{13}]$ yields a flower-like supramolecular precursor ($[MnV_{13}]$-MA) assembled by spines. The $[MnV_{13}]$-MA precursor was then converted to Mn-VN cardoon by nitridation treatment. $[MnV_{13}]$ polyanion was employed to assemble with the rigid ligand melamine (MA) by hydrogen bond and electrostatic interaction due to its high negative charges up to 7 and more surface active oxygen atoms [37,38]. The $[MnV_{13}]$ consists of thirteen $[VO_6]$ octahedrons surrounding a

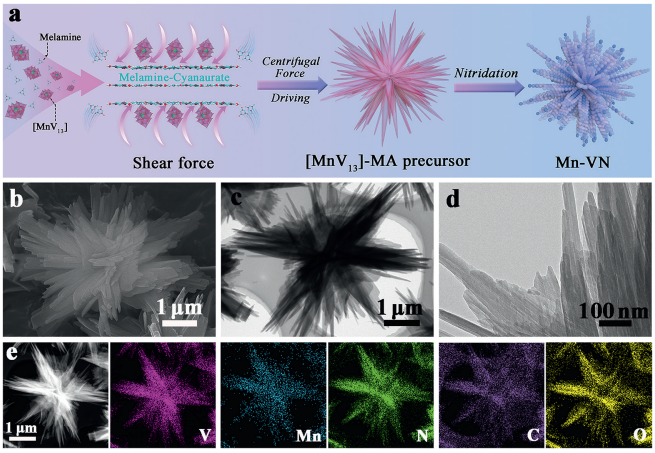

Fig. 1. (a) Schematic illustration of the preparation of Mn-VN cardoon. (b) SEM, (c, d) TEM, (e) STEM images and the corresponding EDS elemental mappings of $[MnV_{13}]$-MA precursor.

central Mn atom (Fig. S1 in Supporting information), providing an opportunity to induce Mn doping in VN. X-ray diffraction (XRD) patterns (Fig. S2 in Supporting information) show the diffraction peaks of $[MnV_{13}]$-MA are different from those of $[MnV_{13}]$, MA and the related mechanical mixture (named as Bulk-$[MnV_{13}]$-MA), suggesting the formation of a new supramolecular assembly. Interestingly, several weak peaks belonging to melamine cyanurate (JCPDS No. 05–0127) appear, indicating that melamine hydrolyzed to generate cyanuric acid, and further reacted with cyanuric acid to form melamine cyanurate [39]. The characteristic peaks of $[MnV_{13}]$ were retained in the as-synthesized $[MnV_{13}]$-MA assembly (Fig. S3 in Supporting information), while a new adsorption peak of 1727 cm^{-1} attributed to C=O, further proves the presence of melamine cyanurate [39,40]. Scanning electron microscopy (SEM) and transmission electron microscopy (TEM) images clearly show $[MnV_{13}]$-MA precursor has a novel 3D hierarchical spines-assembled flower-like morphology (Figs. 1b and c). The transparent characteristic directly evidences the existence of thin layers (Fig. 1d). Energy dispersive spectroscopy (EDS) element mappings (Fig. 1e) indicate the uniform distribution of V, Mn, N, C, and O elements, demonstrating the formation of a unique flaky flower $[MnV_{13}]$-MA precursor. According to the EDS result, the atom ratio of Mn to V is 1.26:10.52, which is quite close to the theoretical ratio of V/Mn in $[MnV_{13}]$ (Fig. S4 in Supporting information). The $[MnV_{13}]$ cluster maintains structural integrity during the process, guaranteeing the reliability of atomic proportion control. In sharp contrast, the precursor (Bulk-$[MnV_{13}]$-MA) synthesized by direct grinding presents an ugly boulder morphology (Fig. S5 in Supporting information). Also, when $[MnV_{13}]$ was replaced by simple ammonium metavanadate (NH_4VO_3), only irregular morphology precursor (V-MA) was obtained (Fig. S6 in Supporting information). The above illustrates the important role of $[MnV_{13}]$ in regulating the assembly process and the final formation of nanoribbon-assembled flowers. As reported, MA easily hydrolyzes to cyanuric acid in acid solution [39]. In this case, $[MnV_{13}]$ solution (pH 5.42) provides an acid environment to promote MA hydrolysis. Then, MA combines with the corresponding hydrolyzed product cyanuric acid and $[MnV_{13}]$, forming spines *via* hydrogen bonding and π-π stacking interactions, which are further assembled into flower-like $[MnV_{13}]$-MA under shear stress induction. When there was no shear stress, irregular thick plates were formed (Fig. S7 in Supporting information). As the stirring rate increases, the morphology changed obviously, meaning that shear stress determines the formation of the assembly structure. The role of shear stress has just been demonstrated in our work to prevent melamine and cyanuric acid from assem-

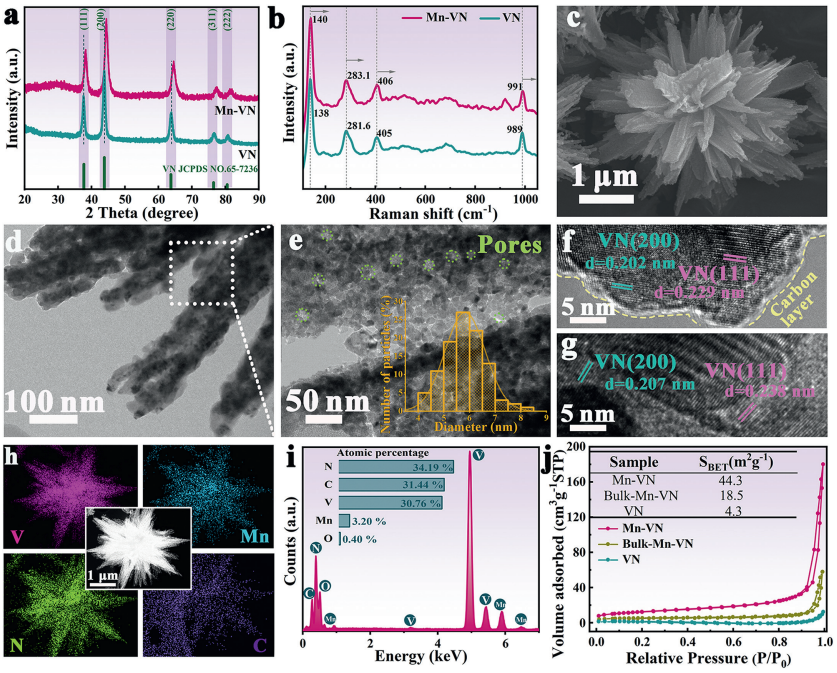

Fig. 2. (a) XRD patterns and (b) Raman spectra of VN and Mn-VN. (c) SEM and (d, e) TEM images of Mn-VN cardoon. HRTEM images of (f) Mn-VN and (g) VN. (h) STEM image and the corresponding EDS elemental mappings of Mn-VN. (i) EDS spectrum and the relative content in atomic percent in Mn-VN. (j) N_2 adsorption/desorption isotherms of different samples.

bling into blocky stacked structure by disrupting stacking interactions between layers [39].

3D hierarchical porous Mn-VN cardoon was prepared by pretreatment with Ar at 350 °C and annealing with NH_3 at 600 °C. All characteristic peaks of Mn-VN are well indexed to the cubic phase of VN (JCPDS No. 65–7236) (Fig. 2a), and no other identifiable peaks associated with manganese species were detected, indicating a complete conversion of [MnV_{13}]-MA precursor to Mn-doped VN. Notably, the diffraction peaks of Mn-VN exhibit slight shift towards higher angles compared to pure VN, due to the replacement of V atoms by smaller Mn atoms, which indicates that Mn is successfully incorporated in the VN lattice. Compared with bulk VN, the wider diffraction peaks of Mn-VN, can be ascribed to the smaller size of Mn-VN. Raman spectrum (Fig. 2b) shows that the characteristic peaks of VN in Mn-VN shift towards higher wavenumber, due to Mn incorporation affects the stretching vibration of V-N bonds, further confirming Mn incorporation causes lattice contraction of VN [16,41]. The SEM image shows Mn-VN inherits the [MnV_{13}]-MA morphology with obvious volume shrinkage (Fig. 2c). It is worth noting that the surface of Mn-VN cardoon presents a rough texture, which is favorable for adsorption during electrocatalysis. TEM images (Figs. 2d and e) show Mn-VN presents coarse nanoribbons with abundant pores, which are composed of well-dispersed small particles (the average size of *ca.* 6 nm). High-resolution TEM (HRTEM) image of Mn-VN exhibits clear lattice fringes with interplanar distances of 0.229 and 0.202 nm (Fig. 2f), smaller than that of (111) and (200) in VN (Fig. 2g), respectively. It indicates that Mn incorporation causes lattice contraction of VN, mainly attributed to the smaller radius of Mn (1.79 Å) compared with V (1.92 Å) [26]. Significantly, a thin carbon layer derived from melamine was observed, which is conducive to stabilizing the catalyst and improving conductivity to accelerate electron transfer during electrocatalysis [42]. STEM image and the corresponding EDX element mappings manifest the uniform distribution of V, Mn, N, and C elements in Mn-VN cardoons (Fig. 2h), further illustrating the successful incorporation of Mn into VN. EDS analysis shows the atomic ratio of Mn to V is approximately 1:9.61 (Fig. 2i), which is almost identical to the ICP result (Table S1 in Supporting information) and close to the ratio in the [MnV_{13}] cluster, further embodying the advantage of polyoxovanadates in precisely targeting metal atomic ratio. In marked contrast to Mn-VN, Bulk-Mn-VN and VN show bulk irregularity morphology with large size aggregated particles (Figs. S8 and S9 in Supporting information), which fully proved that the assembly structure formed by [MnV_{13}] and MA is conducive to inhibiting the aggregation of nitrides. Such 3D hierarchical nanoribbon-assembled cardoons endow Mn-VN with high specific surface area (44.3 m^2/g), significantly higher than Bulk-Mn-VN (18.5 m^2/g) and VN particles (4.3 m^2/g) (Fig. 2j). The far higher value of Mn-VN than that of VN reflects the indispensable role of [MnV_{13}] polyoxovanadate again. This porous hierarchical assembly structure can increase active surface area and facilitate rapid transport of reactants, thereby elevating electrocatalytic activity. Additionally, appropriate synthetic conditions are critical for the construction of 3D hierarchical assembly structured Mn-VN (Figs. S10–S12 in Supporting information).

The elemental compositions and valence states of VN and Mn-VN were analyzed by X-ray photoelectron spectroscopy (XPS) to further probe the electronic structure regulation mechanism after Mn incorporation. Survey spectra demonstrate the coexistence of V, N, C, and O elements in both VN and Mn-VN (Fig. 3a), where the O 1s signal originates from the surface oxidation of nitrides exposed to air. While, the difference is that Mn signal appears in the Mn-VN, further proving the successful doping of Mn. In the Mn 2p spectrum of Mn-VN (Fig. 3b), the deconvoluted peaks centered at 640.0/651.7, 641.1/653.2, and 642.4/654.9 eV are associated with Mn^{2+}, Mn^{3+}, and Mn^{4+} [43]. Mn^{3+} with $t^3_{2g}e^1_g$ electronic configuration has been identified as the active species for water oxidation [26]. High-resolution V 2p XPS spectrum of Mn-VN (Fig. 3c) shows three pairs of peaks at 513.5/520.8, 514.7/522.0, and 516.4/523.8 eV, corresponding to V^{3+}, V^{4+}, and V^{5+}, respectively [20,44]. A positive shift of 0.3 eV is observed in Mn-VN relative to VN, indicating that the electron density on the V element decreases after Mn doping, due to that the incorporation of Mn remodels the electron environment of VN. As shown in Fig. 3d, the N 1s spectrum can be deconvoluted into four peaks centered at binding energies of 396.4, 397.9, 399.3, and 401.1 eV, which are assigned to N–V, pyri-

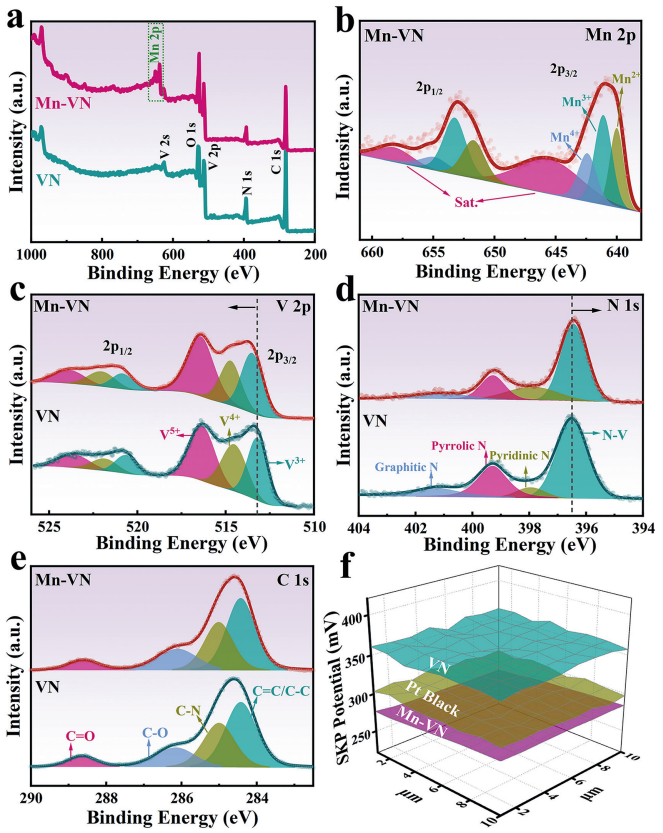

Fig. 3. (a) XPS survey spectra, and high-resolution XPS spectra of (b) Mn 2p, (c) V 2p, (d) N 1s and (e) C 1s for VN and Mn-VN. (f) WF drawings of Pt black, VN and Mn-VN.

dinic N, pyrrolic N, and graphitic N, respectively [45]. The high-resolution C 1s XPS spectrum (Fig. 3e) reveals four peaks at 284.4, 285.0, 286.1, and 288.6 eV, belonging to C–C/C=C, C–N, C–O, and C=O bonds, respectively [46]. Significantly, the N peaks in Mn-VN shifts negatively compared to VN, evidencing the increased electron cloud density around N sites in Mn-VN [44]. The above suggests the incorporation of Mn into the VN lattice and the resulting lattice contraction manipulates electron redistribution. Specifically, Mn with multiple valences can regulate the valence state and electronic structure of V element, enabling electron-rich V to transfer electrons to N. Therefore, Mn doping would increase the electron loss of the V sites, and cause the electron accumulation on the N sites. It is also consistent with the electronegativity order of the elements, *i.e.*, N (3.04) > V (1.63) > Mn (1.55) [25,47]. In this view, Mn incorporation successfully modified the VN by adjusting the crystal environment and electronic structure, thereby optimizing the adsorption behavior of the reactive intermediates, and thus improving catalytic activity. In fact, in terms of pure VN, the higher electronegativity of N than V makes the V atoms electron-deficient (electrophilic). Interestingly, Mn incorporation induces V sites further loss more electrons, making it more electrophilic and easier to bind O-containing intermediates, which favors the OER/UOR process. To further determine the effect of electron density on the catalytic process, the work functions are calculated to be 5.70, 5.62, and 5.65 eV for VN, Mn-VN, and Pt black, respectively, based on scanning Kelvin probe measurement (Fig. 3f). Compared with pure VN, the lower work function of Mn-VN, which is closer to Pt, indicates the higher charge carrier concentration near the Fermi level, responsible for its promoted electron transferability, and the increased electrical conductivity [30]. Mn-VN possesses exclusive ability to trap electrons like Pt black, perhaps accounting for the increased HER catalytic activity.

As previously mentioned, nanoribbon-assembled hierarchical porous structure, and Mn-incorporation induced electronic structure regulation render Mn-VN cardoon a promising robust electrocatalyst, which was further verified by experiments. The electrocatalytic performances of Mn-VN, Bulk-Mn-VN, pure VN, and Pt/C catalysts toward HER were evaluated in 1 mol/L KOH using a typical three-electrode system. Fig. 4a displays the polarization curves obtained by linear sweep voltammetry (LSV) test after 95% iR compensation. Mn-VN cardoon can achieve current densities of 10, 50, and 100 mA/cm^2 with low overpotentials of only 86, 159, and 191 mV, much lower than those of Bulk-Mn-VN (178, 256, and 293 mV) and VN (226, 305, and 355 mV), respectively. Noticeably, the activity of Mn-VN is better than that of Pt/C, when current density exceeds 260 mA/cm^2. Fig. 4b visually compares the overpotentials of various electrodes, in which the same potential trend as above can be observed at higher current densities (Table S2 in Supporting information), indicating the Mn-VN presents a significantly enhanced HER activity compared to Bulk-Mn-VN and VN. Moreover, the electrocatalytic HER performance of the Mn-VN cardoon surpasses that of most VN-based materials (Table S3 in Supporting information). To elucidate the electrocatalytic kinetic mechanism, Tafel slope was analyzed by fitting the linear segment of the Tafel plot. As presented in Fig. 4c, the Mn-VN cardoon possesses a Tafel slope of 58 mV/dec, which is much lower than that of Bulk-Mn-VN (124 mV/dec) and VN (135 mV/dec), indicating its faster electrode reaction kinetics. The HER kinetic mechanism of the Mn-VN cardoon follows the Volmer–Heyrovsky mechanism, where electrochemical desorption is identified as the rate-limiting step [5]. Compared with VN, the significantly reduced Tafel slope indicates that the sluggish Volmer step of VN is greatly accelerated after Mn incorporation, highlighting the advantage of Mn incorporation. The exchange current density (j_0) of Mn-VN cardoon is determined to be 0.741 mA/cm^2, much higher than that of Bulk-Mn-VN (0.414 mA/cm^2) and VN catalysts (0.325 mA/cm^2), revealing the higher excellent kinetics characteristics of Mn-VN toward HER (Fig. S13 in Supporting information). Such remarkable enhanced activity of Mn-VN cardoon is closely related to its inherent characteristics. Electrochemical impedance spectroscopy (EIS) tests (Fig. 4d) reveal that Mn-VN cardoon delivers a low charge transfer resistance (R_{ct}) of about 4.5 Ω, much lower than the reference samples, Bulk-Mn-VN (≈7.5 Ω) and VN (≈12.0 Ω), suggesting that Mn-VN cardoon possesses faster charge transfer with reactants/intermediates during the HER. Interestingly, both Mn-VN cardoon and Bulk-Mn-VN show lower R_{ct} compared to VN, implying that Mn incorporation in VN significantly improves electrical conductivity by adjusting the electronic structure. The catalytic activity strongly depends on the number of the exposed active sites and the inherent activity [29]. Therefore, the electrochemical active surface area (ECSA) was further determined by measuring double-layer capacitance (C_{dl}) (Fig. 4e and Fig. S14 in Supporting information), which can evaluate the number of accessible active sites. The order of C_{dl} values for different catalysts is Mn-VN cardoon (208.3 mF/cm^2) > Bulk-Mn-VN (118.7 mF/cm^2) > VN (31.4 mF/cm^2). As C_{dl} value is directly proportional to ECSA, the Mn-VN cardoon has the largest ECSA (Fig. S15a in Supporting information), which is approximately 6.6 and 1.8 times that of VN and Bulk-Mn-VN, respectively, suggesting that Mn-VN could expose more active sites during HER. The above implies that both Mn incorporation and morphology engineering play important roles in creating/exposing more active sites, and thus improving HER performance. What is more, through careful comparison, the incorporation of Mn in the VN lattice appeared to have even far more impact than morphology engineering in increasing active sites. Furthermore, the ECSA-normalized LSV curves (Fig. S15b in Supporting information) indicate that the Mn-VN cardoon catalyst exhibits a higher j_{ECSA} than the others at the same potential, suggesting higher intrinsic activ-

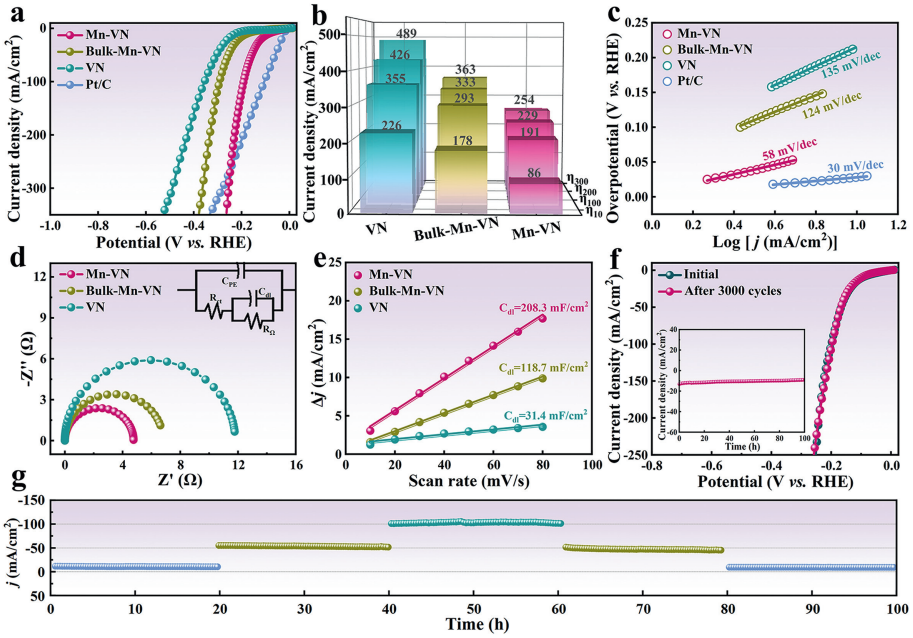

Fig. 4. (a) LSV curves. (b) Comparison of overpotentials at different current densities. (c) Tafel plots. (d) Nyquist plots and (e) estimation of C_{dl} by plotting the current density variation ($\Delta j = (j_a - j_c)/2$) in 1 mol/L KOH of different samples. (f) LSV curves of Mn-VN before and after 3000 cycles. Insert: *I-t* curve for Mn-VN. (g) Multi-step chronoamperometric curves for Mn-VN.

ity of the individual active site in Mn-VN cardoon, which benefits greatly from morphology tailoring and electronic structure regulation by Mn incorporation [36]. The superiority of Mn incorporated VN for HER were further confirmed by density functional theory (DFT) calculations (Fig. S16 in Supporting information). Long-term stability is another key criterion to evaluate whether the electrocatalytic performance of catalysts is suitable for practical applications. As displayed in Fig. 4f, the polarization curve of Mn-VN cardoon after 3000 CV cycles is nearly identical to the initial one. The chronoamperometric test shows that a slightly decay in current density emerged after 100 h operation. Moreover, multi-step chronoamperometric curves of Mn-VN under various current density display each step remains nearly no notice change (Fig. 4g), indicating a predominant mechanical robustness [48]. These results verify the excellent electrochemical stability of Mn-VN cardoon for HER catalysis. Moreover, XRD, SEM, TEM images, and XPS spectra (Figs. S17 and S18 in Supporting information) demonstrate that the crystal structure, morphology and chemical state of Mn-VN are well maintained after durability test. The dependence of HER activity on [MnV_{13}] amount and calcination temperature were also investigated (Figs. S19 and S20 in Supporting information). The above results strongly confirm that the significant influence of hierarchical structured morphology and electron structure regulation induced by Mn incorporation on the catalytic activity.

The UOR performances of the as-prepared catalysts were evaluated in 1 mol/L KOH with 0.5 mol/L urea *via* a typical three-electrode system without iR-correction. Fig. 5a exhibits the LSV curves of the Mn-VN electrode in 1 mol/L KOH with or without 0.5 mol/L urea. In sharp contrast to OER, the UOR plot exhibits a rapidly rising anodic current density over applied potential, and much lower applied potential than that for OER to reach the same current density. Concretely, the UOR only requires 1.346 and 1.366 V to reach the current density of 10 and 50 mA/cm^2, respectively, whereas OER needs much higher potential values (1.551 and 1.625 V), indicating that UOR catalysis is more favorable than OER. Moreover, the much lower Tafel slope of UOR (46 mV/dec) compared to OER further supports the faster UOR kinetics (Fig. S21 in Supporting information). Obviously, the greatly decreased potentials of 205 and 259 mV at 10 and 50 mA/cm^2 confirms the advantage of UOR over OER, which means that energy can be considerably saved for hydrogen production through UOR. Similarly, the UOR activities of pure VN, Bulk-Mn-VN and RuO_2 were also probed for comparison (Fig. 5b). Mn-VN exhibits higher UOR activity than Bulk-Mn-VN (1.367 V@10 mA/cm^2), VN (1.393 V@10 mA/cm^2), and RuO_2 (1.374 V@10 mA/cm^2) (Table S4 in Supporting information). At an applied voltage of 1.366 V, the current density of the Mn-VN is 17.2 and 5.1 times higher than that of VN and Bulk-Mn-VN, respectively, suggesting both Mn incorporation and morphology engineering play key roles in improving performance, and Mn incorporation is the dominant factor. Similarly, the Tafel slope of Mn-VN for the UOR process is calculated as 46 mV/dec, which is lower than those of pure VN (157 mV/dec) and Bulk-Mn-VN (91 mV/dec), suggesting the enhanced reaction kinetics of Mn-VN for UOR (Fig. 5c). The kinetics superiority of this catalyst can be further investigated *via* EIS measurement. According to the Nyquist plot illustrated in Fig. 5d, the Mn-VN catalyst displays apparently decreased R_{ct} of 1.6 Ω, compared to VN (5.1 Ω) and Bulk-Mn-VN (3.2 Ω), signifying a faster electron-transfer capability of the Mn-VN cardoons. In this case, Mn incorporation induces the improvement of electrical conductivity by electronic structure modulation, while morphology engineering promotes charge transfer at the electrode/electrolyte interface [49]. The C_{dl} value of the Mn-VN (8.18 mF/cm^2) catalyst is higher than that of VN (2.92 mF/cm^2) and Bulk-Mn-VN (3.85 mF/cm^2) (Fig. S22 and Table S4 in Supporting information). The ECSA values of Mn-VN, Bulk-Mn-VN and VN are 204.5, 96.3, and 73.0 cm^2, respectively (Fig. S23a in Supporting information), which manifests that Mn-incorporation and morphology engineering enable Mn-VN to dramatically expose more active sites. Accordingly, Mn-VN delivers largest current density at the same potential from the ECSA-normalized LSV curves (Fig. S23b in Supporting information), implying the highest intrinsic activity of the Mn-VN cardoons. According to DFT calculations, the adsorption energy of urea for the Mn site and V site of Mn-VN is −0.639 and −0.301 eV, respectively, which is more negative than that of VN (−0.230 eV) (Fig. S24 in Supporting information). It indicates that Mn can serve as the center of catalytic activity. Urea

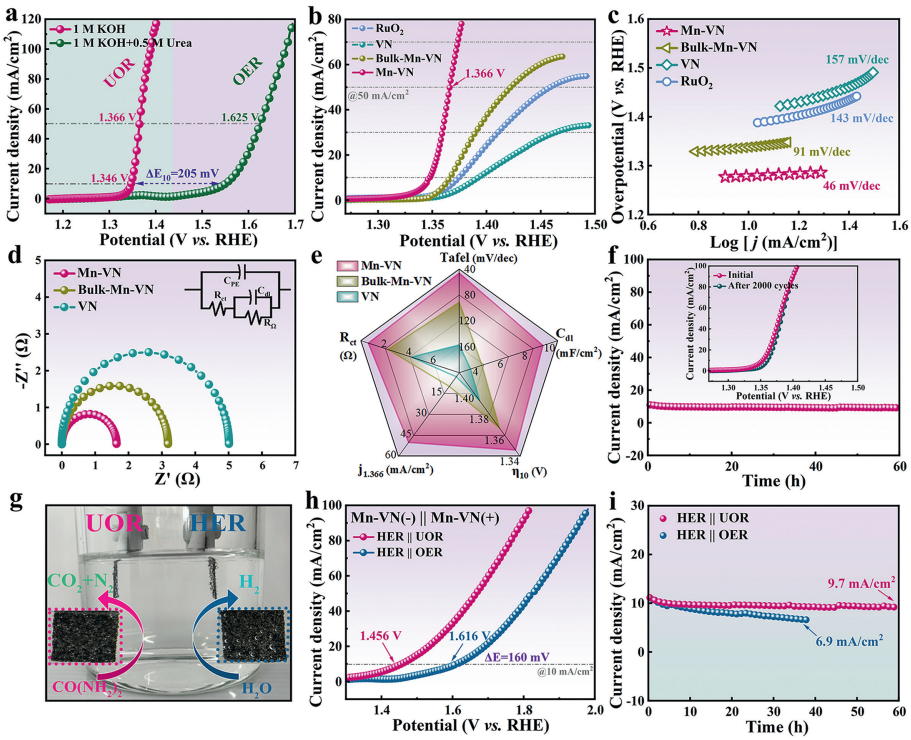

Fig. 5. (a) LSV curves of Mn-VN with and without urea. UOR electrochemical tests of different samples in 1 mol/L KOH + 0.5 mol/L urea: (b) LSV curves, (c) Tafel plots, (d) Nyquist plots, (e) comprehensive performance comparison, (f) *I–t* chronoamperometric curve of Mn-VN. Insert: LSV curves before and after 2000 cycles. (g) The magnified photos of electrolyzer. (h) LSV curves of the Mn-VN couple in 1 mol/L KOH with and without urea in a two-electrode system. (i) *I-t* curves of urea-assisted water electrolysis and traditional water electrolysis.

molecules can be easily adsorbed and activated on the surface of the Mn-VN catalyst to further promote the UOR process. The comparison of the catalysts in Fig. 5e clearly demonstrates that Mn-VN has the best electrocatalytic performance for UOR. In addition, the remarkable UOR activity of Mn-VN in 0.5 mol/L urea also surpasses many reported materials (Table S5 in Supporting information). Therefore, we can draw a conclusion that constructing Mn-doped VN hierarchical porous structure not only increases the active sites but also improves the intrinsic catalytic activity. Previous XPS result validates that Mn incorporation plays a leading role in electron structure modulation, which is expected to optimize urea adsorption, as certified by theoretical calculations [27]. Stability is another critical aspect of assessing the catalyst performance. The long-term *I–t* curve in Fig. 5f exhibits no significant decrease in the electrocatalytic UOR activity of Mn-VN over 60 h. Simultaneously, a slight potential increase was observed in the LSV curves after 2000 CV. The above illustrates its excellent stability. A series of characterization examinations of Mn-VN after the UOR process were carried out to further clarify the origin of the stability, considering that the reconstructed structure of the transition metal-based catalyst is usually the true catalytic species [28,50]. No significant change in XRD patten is indicative of the well-preserved crystal structure before and after the UOR process. The hierarchical porous cardoon morphology of Mn-VN is basically maintained after UOR, but the initial surface nanoribbons are slightly damaged, resulting in more rough edges (Fig. S25 in Supporting information). Such unique structure favors the exposure of more active sites and provides a larger surface area, thereby accelerating mass transfer and bubble release, which is conducive to UOR kinetics [12]. The new lattice fringes of 0.221 and 0.249 nm belonging to (121) and (021) planes of VOOH appear, demonstrating that VN transforms into high-valence V-oxides during UOR [51,52]. The corresponding EDS elemental mapping further confirms an increase in the content of O element from 0.40% (initial) to 3.35% (after UOR) (Fig. S26 in Supporting information). Moreover, the content of V element in Mn-VN decreases, suggesting the dissolution of trace V species at the surface, which is responsible for the collapse of the nanoribbons. XPS results (Fig. S27 in Supporting information) reveal V^{3+} tends to decrease along with a slight increase in V^{4+} and V^{5+}, and the Mn^{2+} peak intensity is reduced, which means the surface reconstruction occurs during the UOR. Furthermore, the strong M–O and M–OH bonds in the O 1s XPS spectrum further verify the increase of metal valence caused from the conversion of VN into VOOH. A conclusion can be drawn that the surface of Mn-VN was corroded and partially oxidized to generate the corresponding oxide/oxy(hydroxide) species, which could further optimize the oxidative activity. Thus, the surface oxidation reconstruction and the produced high-valence V-oxides on the surface of Mn-VN are the real active sites for UOR.

It is noteworthy to point out that the Mn-VN also exhibits excellent HER performances after adding 0.5 mol/L urea (Fig. S28 in Supporting information). In this regard, a urea assisted water electrolyzer for hydrogen production was configured by using Mn-VN as both the anode and cathode (Fig. 5g). Urea-assisted water electrolysis delivers higher current density than conventional water electrolysis at the same cell voltage (Fig. 5h). The voltage required for urea electrolysis is 160 mV lower than that of water electrolysis when operated at 10 mA/cm^2, implying that replacing OER with UOR is a highly effective approach for energy-saving hydrogen production. The present Mn-VN(-)||Mn-VN(+) system is also highly competitive with the recently reported noble-free catalysts for urea-assisted overall-water splitting (Table S6 in Supporting information). The durability test of the urea-assisted water electrolyzer and conventional water electrolyzer were conducted using chronoamperometry at 10 mA/cm^2 (Fig. 5i). It is worth noting that the voltage change of urea-assisted water electrolyzer is negligible in the case of continuous electrolysis over 60 h, which emphasizes the distinguished durability of Mn-VN cardoons. Based on the

abovementioned results, Mn-VN has a good application prospect in the urea-assisted overall water splitting for sustainable H_2 production, where replacing OER with UOR can effectively reduce energy consumption.

In summary, we have triggered precise Mn incorporation in the VN lattice by virtue of polyoxovanadate [MnV_{13}], in parallel with constructing a special 3D porous hierarchical assembly architecture Mn-VN cardoon, achieving synchronous morphology engineering and electronic structure modulation. Accordingly, the as-obtained Mn-VN catalyst can catalyze HER and UOR efficiently, in which Mn incorporation cause the lattice contraction of VN, leading to electron redistribution, as verified by the XPS and work function analysis. Impressively, the electrolyzer composed of Mn-VN electrodes for urea-assisted water splitting requires a low cell voltage of 1.456 V at 10 mA/cm^2, which can be reduced by 160 mV compared to the traditional overall water splitting electrolyzer. The strategy is of great value for designing 3D hierarchical assembly architecture catalysts with precise metal incorporation, and corroborating the positive contribution of electronic modulation to improving the electrocatalytic capacity for energy-saving hydrogen production in urea-rich wastewater.

Declaration of competing interest

The authors declare that they have no known competing financial interests or personal relationships that could have appeared to influence the work reported in this paper.

CRediT authorship contribution statement

Hongyang Li: Writing – original draft, Methodology, Data curation, Conceptualization. **Yue Liu:** Data curation, Formal analysis. **Xiuwen Wang:** Investigation, Formal analysis. **Haijing Yan:** Writing – review & editing, Funding acquisition. **Guimin Wang:** Formal analysis. **Dongxu Wang:** Investigation. **Yilong Wang:** Formal analysis. **Shuo Yang:** Formal analysis. **Yanqing Jiao:** Writing – review & editing, Writing – original draft, Supervision, Funding acquisition, Conceptualization.

Acknowledgments

This research was supported by the National Natural Science Foundation of China (Nos. 22322104, 22171074), the Natural Science Foundation of Heilongjiang Province (No. YQ2021B009), the Reform and Development Fund Project of Local University supported by the Central Government (Outstanding Youth Program), Heilongjiang Province Young Scientific and Technological Talent Lifting Project (No. 2023QNTJ019), the Basic Research Support Project for Outstanding Young Teachers in Heilongjiang Provincial University (No. YQJH2023129), the Outstanding Youth Science Foundation of Heilongjiang University (No. JCL202301).

Supplementary materials

Supplementary material associated with this article can be found, in the online version, at doi:10.1016/j.cclet.2024.110042.

References

[1] Y. Zhang, J. Liu, S.L. Li, et al., Energy Chem. 1 (2019) 100021.
[2] H.G. Cha, K.S. Choi, Nat. Chem. 7 (2015) 328–333.
[3] Z.W. Seh, J. Kibsgaard, C.F. Dickens, et al., Science 355 (2017) eaad4998.
[4] Y.K. Zhang, Y.X. Lin, T. Duan, et al., Mater. Today 48 (2021) 115–134.
[5] Y. Jiao, Y. Zheng, M. Jaroniec, et al., Chem. Soc. Rev. 44 (2015) 2060–2086.
[6] R. Yang, X.Z. Shi, Y.Y. Wang, et al., Chin. Chem. Lett. 33 (2022) 4930–4935.
[7] G.C. Yang, Y.Q. Jiao, H.J. Yan, et al., Nat. Commun. 13 (2022) s41467.
[8] S. Xu, X.W. Ruan, M. Ganesan, et al., Adv. Funct. Mater. 34 (2024) 2313309.
[9] W.S. Tang, L.N. Zhang, T.Y. Qiu, et al., Angew. Chem. Int. Ed. 62 (2023) e202305843.
[10] P. Guo, S.F. Cao, W.J. Huang, et al., Adv. Mater. 36 (2024) 2311766.
[11] S.K. Geng, Y. Zheng, S.Q. Li, Nat. Energy 6 (2021) 904–912.
[12] S. Chen, J.J. Duan, A. Vasileff, et al., Angew. Chem. Int. Ed. 55 (2016) 3804–3808.
[13] X.T. Gao, S. Zhang, P.T. Wang, et al., Chem. Soc. Rev. 53 (2024) 1552–1591.
[14] S.L. Wang, J.Y. Zhu, X. Wu, et al., Chin. Chem. Lett. 33 (2022) 1105–1109.
[15] L.W. Lin, S.Q. Piao, Y.J. Choi, et al., Energy Chem. 4 (2022) 100072.
[16] Y. Zhong, D.L. Chao, S.J. Deng, et al., Adv. Funct. Mater. 28 (2018) 1706391.
[17] S.Q. Li, X. Sun, Z.H. Yao, et al., Adv. Funct. Mater. 29 (2019) 1904780.
[18] W.Q. Jia, B.W. Liu, R. Gong, et al., Small 19 (2023) 2302025.
[19] Y. Wang, Y.Q. Jiao, H.J. Yan, et al., Angew. Chem. Int. Ed. 61 (2022) e202116233.
[20] X. Dong, H.J. Yan, Y.Q. Jiao, et al., J. Mater. Chem. A 7 (2019) 15823–15830.
[21] H.J. Yan, Y. Xie, A.P. Wu, et al., Adv. Mater. 31 (2019) 1901174.
[22] M.R. Kandel, U.N. Pan, P.P. Dhakal, et al., Small 20 (2023) 2307241.
[23] L.X. Dai, Y. Wang, L. Sun, et al., Adv. Sci. 8 (2021) 2004995.
[24] Y. Liu, L. Bai, Q.Q. Jia, et al., Chin. Chem. Lett. 34 (2023) 107855.
[25] W.M. Li, R. Liu, G.T. Yu, et al., Small 20 (2023) 2307164.
[26] L. Li, J. Zhou, X. Wang, et al., Adv. Mater. 35 (2023) 2302966.
[27] F. Chen, F. Yang, C. Sheng, et al., J. Colloid Interface Sci. 626 (2022) 445–452.
[28] P. Li, Y.Q. Huang, Q.H. Huang, et al., J. Energy Chem. 87 (2023) 479–490.
[29] Y.Q. Jiao, H.J. Yan, C.G. Tian, et al., Acc. Mater. Res. 4 (2022) 42–56.
[30] Y.Q. Jiao, H.J. Yan, R.H. Wang, et al., ACS Appl. Mater. Interfaces 12 (2020) 49596–49606.
[31] D. He, L. Cao, L. Feng, et al., Chin. Chem. Lett. 33 (2022) 4781–4785.
[32] Y.Y. Ma, Z.L. Lang, L.K. Yan, et al., Energ. Environ. Sci. 11 (2018) 2114–2123.
[33] Y.C. Bai, H. Zhang, B. Xiang, et al., Nano Energy 89 (2021) 106386.
[34] Z.X. Xu, X.D. Zhuang, C.Q. Yang, et al., Adv. Mater. 28 (2016) 1981–1987.
[35] C.R. Xu, J.L. Mu, T. Zhou, et al., Adv. Funct. Mater. 32 (2022) 2206501.
[36] Y. Gu, A.P. Wu, Y.Q. Jiao, et al., Angew. Chem. Int. Ed. 60 (2021) 6673–6681.
[37] W.L. Li, E.F. Ni, X.H. Li, et al., T. Nonferr. Metal. Soc. 26 (2016) 2372–2379.
[38] Y.N. Zhao, W.L. Li, Y.Q. Li, et al., Adv. Funct. Mater. 33 (2023) 2306598.
[39] Q. Li, Y.Q. Jiao, Y.Q. Tang, et al., J. Am. Chem. Soc. 145 (2023) 20837–20848.
[40] T.C. Liu, J.X. Ge, Y. Xu, et al., Energy Storage Mater. 32 (2020) 261–271.
[41] H. Jiang, M.Z. Sun, S.L. Wu, et al., Adv. Funct. Mater. 31 (2021) 2104951.
[42] W. Zhang, H.J. Yan, Y. Liu, et al., J. Mater. Chem. A. 11 (2023) 15033–15043.
[43] X.M. Li, Q.Y. Hu, H.Y. Wang, et al., Appl. Catal. B 292 (2021) 120172.
[44] J.Z. Feng, R.X. Tang, G.F. Liu, et al., Chem. Eng. J. 452 (2023) 139131.
[45] Y.Q. Jiao, H.J. Yan, D.X. Wang, et al., Sci. China Mater. 65 (2022) 1225–1236.
[46] H.J. Yan, Y. Xie, Y.Q. Jiao, et al., Adv. Mater. 30 (2017) 1704156.
[47] J.C. Hao, Z.C. Zhuang, K.C. Cao, et al., Nat. Commun. 13 (2022) s41467.
[48] Y. Li, Y.Q. Jiao, H.J. Yan, et al., Angew. Chem. Int. Ed. 62 (2023) e202306640.
[49] C.C. Li, Y.W. Liu, Z.W. Zhuo, et al., Adv. Energy Mater. 8 (2018) 1801775.
[50] M. Yang, Y.M. Jiang, M.J. Qu, et al., Appl. Catal. B 269 (2020) 118803.
[51] J. Zhang, R.J. Cui, C.C. Gao, et al., Small 15 (2019) 1904688.
[52] W.B. Li, J.F. Huang, L.L. Feng, et al., J. Mater. Chem. A 5 (2017) 20217–20227.